LOCAL SCALE ATMOSPHERIC TRANSPORT MODELING FOR THE QUANTIFICATION OF METHANE EMISSIONS FROM INDUSTRIAL AND LANDFILL SITES

A M2 INTERNSHIP REPORT

MASTER OF SCIENCE
in
PHYSICS OF COMPLEX SYSTEMS

Submitted by

SAMUEL TAMAGNONE

Under the supervision of

PRAMOD KUMAR

GRÉGOIRE BROQUET

and co-supervision of

ALESSANDRO PELIZZOLA

PHYSICS DEPARTMENT
UNIVERSITÉ PARIS-SACLAY - POLITECNICO DI TORINO

Laboratoire des Sciences du Climat et de l'Environnement

JUNE, 2022

ACKNOWLEDGEMENT

First and foremost, I would like to thank both my supervisors Pramod Kumar and Grégoire Broquet. Pramod thought me the most important concepts of numerical simulations in the atmosphere, provided me with interesting material and was always ready to answer my questions related to many technical aspects of this work. Grégoire introduced me to his team making me feel part of it and followed my work, raising important points and providing useful insights during all my internship. Also, I reserve a special thank to my family for their support during my years as a student. Without that support I could not have had the same experiences as I did. Last but not least, I would like to thank Adil Shah for being passionately dedicated in the measurement campaigns and Philippe Ciais and Olivier Laurent for being responsible with Grégoire for the TRACE project.

This work was supported by the Chaire Industrielle Trace ANR-17-CHIN-0004-01 co-funded by the ANR French national research agency, TotalEnergies-Raffinage Chimie, SUEZ, and THALES ALENIA SPACE.

Paris Samuel Tamagnone

October 13, 2022

Abstract

Accurate atmospheric monitoring of methane (CH_4) emissions from industrial and waste processing sites such as landfills is essential to reduce their emissions. The monitoring of CH_4 emissions from these sites often relies on local scale atmospheric transport models to simulate concentrations associated to the plume from a source with a given emission rate. In recent years, a growing interest in estimating CH_4 emissions has led to the development of different atmospheric inversion frameworks based on stationary or mobile measurements and on transport modeling. The most commonly used model for atmospheric inversions at local-scale is the simple Gaussian model. Here, we investigate the power of a more complex model and compare the results with the Gaussian one. Large Eddy Simulations (LES) models are a promising tool for simulating the realistic CH_4 concentration plumes from industrial and landfill sites. They are more versatile than the simple Gaussian model, because they can simulate the time evolution of the turbulent flow and the effects of a complex topography, and can be used not only for simulating the averaged data, but also for realizing high frequency "virtual measurements". In this study, we utilized a LES model to simulate the CH_4 plume dispersion from a point source controlled CH_4 release in an industrial environment and from multiple complex area sources in a landfill. We characterize the LES of flow and plume dispersion by studying their convergence properties and their performance. The *in-situ* atmospheric CH_4 mole fraction measurements from stationary and mobile sensors from the controlled methane release experiments are used as a benchmark of the LES model. For the landfill site, we use *in-situ* mobile measurements from a campaign and the LES simulations of plumes from the potential emission sources to estimate the total methane emission of the landfill. The inversion results for the landfill site with LES simulations are compared with those estimated by using a Gaussian plume model. The order of magnitude of the estimated landfill emissions obtained with the two transport models are found to be comparable, but the details of the transport are different when we deal with a complex topography. Future studies will be carried out to better exploit the high frequency data produced with LES. At this stage, we use only a coarse grid resolution for LES simulations of landfill plumes due to high computational cost, a grid sensitivity analysis will be conducted for better characterization of flow and plume dispersion.

Contents

List of Tables

List of Figures

Chapter 1

INTRODUCTION

1.1 The importance of industrial methane emission monitoring

The reduction of greenhouse gases (GHG) emission is of vital importance in the context of mitigation of climate change. Methane (CH_4) is the second most important GHG just after carbon dioxide (CO_2), if we consider anthropogenic emissions. Releasing 1 kg of CH_4 in the atmosphere produces the same impact on global warming as 28 Kg of CO_2 [3]. Due to its relatively short lifetime, reduction of CH_4 can have more immediate positive effects with respect to other GHG [4]. Studies of global CH_4 emission rates show that they have risen from approximately 15 Tg/yr to 20 Tg/yr in the period from 2007 to 2014 [5] and about 60% of those (range of 50-70%) are from an anthropogenic origin [6]. The most impacting sources are waste-processing plants (wastewater treatment plants and landfills), oil, coal and gas extraction sites and farms. Industries must list their emissions through national inventory reports and some have to commit to reduce them. However, the choice of appropriate mitigation policies and the verification of their effectiveness relies on a proper quantification of the emission rates and on the localization of the sources. Usually, emission sources from industrial sites are spread heterogeneously on the site and the site itself can have a complex topography, this increases the challenges in providing precise estimates. Therefore until recently, the majority of the estimates of the emission rates were based on scale factors times the quantity of gas and oil produced or of waste processed, this often caused an underestimation of such rates. Recent approaches use *in-situ* stationary and/or mobile measurements with atmospheric transport models in the atmospheric inversions to localize and quantify the methane emissions at local scale [7]. Due to the high cost of CH_4 sensors, a great effort is being done in modeling and analyzing the outcome of near-surface mobile measurements, in order to cover larger areas with fewer sensors [2]. In order to better exploit measurements from a few stationary sensors, more accurate local dispersion modeling is needed.

In the framework of the TRAcking Carbon Emissions program (TRACE program https://trace.lsce.ipsl.fr/) at Laboratoire des Sciences du Climat et de l'Environnement (LSCE; UVSQ-CEA-CNRS) with collaboration of Laboratoire de Meteorogie Dynamique (LMD; CNRS-Ecole Polytechnique) and industrial partners Thales Alenia Space, SUEZ and TotalEnergies, we investigate new GHG emissions measurements and atmospheric inversion methods from the scale of an industrial site up to national and global GHG budgets. The program has three main objectives: creating a long-term partnership between three major industries and leading researchers, training young scientists and industrial staff, developing innovative methods to monitor greenhouse gases emissions to support

effective mitigation actions in different economic sectors. In particular, a large component of TRACE is dedicated to the monitoring of CH_4 emissions from industrial sites based on mobile and fixed station CH_4 measurements deployed on targeted sites, and on local scale atmospheric transport inverse modeling.

1.2 Scope of the study

The general framework for estimating emissions with an atmospheric inversion approach is based on three main components [8]: the observations of CH_4 mole fractions, based on measurements from fixed or mobile sensors, information on meteorological data (wind speed/direction, temperature etc.) and on possible sources location and strength, and a dispersion model to simulate the mole fractions enhancements associated to a given source rate and location or spread. Using an appropriate optimization approach, one gets the optimal parameters of the model and thus finds an estimate for the source strength and sometimes location. The majority of the studies conducted within the TRACE program up to now made use of the Gaussian model. This model has the great advantages of being very versatile for different systems and of providing fast results even with poor computational resources. Though it has two major drawbacks. First, its use is not justified in sites with a complex (not flat) topography and second, it assumes stationary and homogeneous conditions. The objective of this study is thus to understand if we can obtain more accurate modeling results using a more complex model. In particular, we investigated the application of the Large Eddy Simulations (LES) model to accurately model the flow field and transport of methane plumes in a site with a complex topography and also to access how accounting for the variations in time of wind and thus plume helps better fitting the data in atmospheric inversion. To realize the LES we have used the PALM model, developed at the Hannover University [9]. We set up the model for two different sites. The first one is an industrial site owned by TotalEnergies located in Lacq, France. In October 2019, this site was used to produce an intensive campaign of controlled release experiments to which we participated in framework of TRACE program [2]. The meteorological data measured on 02-10-2019 will be used to setup a LES to evaluate the PALM model performance using the methane mole fraction measurements, when fed with actual location and rate of the releases of a controlled experiment. The second one is a landfill, owned by the SUEZ, located in Amailloux, western France. For this site, by using the real topography of the landfill, we will perform the LES simulations of flow-field and methane plumes from potential emission sources for a mobile measurement campaign on 24-03-2021. With this simulation, we then check how much inverted methane emissions based on LES differ from that with the Gaussian model and whether with the LES model we can obtain a better fit of the observed mole fraction.

1.3 Outline

The outline of this study is organised as follows.

In Chapter 2, we briefly presented the governing flow and transport equations of the PALM LES model [10] and the formulation of a Gaussian plume model [2] used in this study.

Chapter 3 presents a detailed description of the measurements from the controlled methane release experimental campaign in the industrial environment and a near-surface

mobile measurement campaign conducted at the landfill site used in this study.

In chapter 4, we describe in detail the numerical schemes and the simulation setup used for both sites. This chapter also presents the new development that we have performed on the original PALM source code to perform LES plume simulations with area sources of any desired shape, a feature that did not exist in the default code. Eventually, we explain the detailed study of convergence of the LES model simulations with respect to the size of the grid boxes, the size of the whole domain, and the simulation time.

Chapter 5 presents the results of the performance evaluation of the PALM model wind and plume simulations using the data of the Lacq experiment. We evaluate the LES simulation of the wind field with the measurements conducted at a fixed meteorological station by comparing average values, standard deviations, and rapidity of variability for wind speed and direction. Moreover, we compare the averaged and high-frequency near-instantaneous CH_4 mole fractions from the LES simulations with the data at the fixed tripods and near-instantaneous data from the instruments in a moving car. We use these comparisons to calculate the model error and check if the performance is better than that of the Gaussian model. For the landfill site, we compare the simulated and observed wind field at a fixed station, and then the simulated CH_4 mole fractions are used in an inversion approach to quantify the methane emission of the landfill. We compare the estimated emissions using LES simulations with the results obtained with the less costly Gaussian model.

In Chapter 6 we discuss the possible continuations to this study and future routes to be explored.

Chapter 2

MODELS FOR METHANE TRANSPORT

2.1 The PALM LES model

The Gaussian model, as we will see in the next section, describes average behaviour of plumes in stationary conditions, but it provides no information on the time evolution of a tracer dispersed into the atmosphere. Moreover the Gaussian model is applicable for plume dispersion mostly in homogeneous terrains. CH_4 leaks from industrial sites can occur over highly irregular topographies, in such domain the Gaussian model assumptions no longer hold and its accuracy can be severely hampered. For these reasons. Computational fluid dynamics (CFD) models are better suitable for flow-field and plume dispersion in complex terrains. In this study, we have utilized a Large Eddy Simulations (LES) model. LES models have a much higher computational cost with respect to the Gaussian model, as a Gaussian model computation is performed in a few seconds, while LES take tens of hours to run, but they are much more reliable when treating complex domains. In this study, we used the LES model PALM (PALM Model System version 21.10) for simulations of methane plumes from point and area sources in both homogeneous and complex terrains.

PALM is an advanced state-of-the-art meteorological modeling system for atmospheric and oceanic boundary layer, developed at the Hannover University [9]. The main idea behind the model is to treat large scales and small scales separately: large eddies, that contain most of the energy of the flow, are explicitly resolved. The impact of small eddies on the large-scale flow is parameterized using a subgrid scale model. The accuracy increases when smaller and smaller eddies are resolved in high resolution LES simulations, but so does the computational cost. A spectral cut is performed at a wavelength Δ, chosen by the user, structures larger than Δ are explicitly resolved, structures smaller than Δ (subgrid scales) are filtered out. The filter procedure removes the small scales from the model equations, but it produces new unknowns, mainly averages of fluctuation products. These unknowns describe the effect of the unresolved, small scales on the resolved, large scales; they are included in the model through a parameterization that uses information from the resolved scales. By default, PALM has six prognostic quantities: the velocity components u, v, w, on a Cartesian grid, the potential temperature θ, specific humidity q_V or a passive scalar s, and the subgrid scale turbulent kinetic energy (SGS–TKE) e. The set of equations solved at the resolved scales is the one used in most of the CFD models and it corresponds to Boussinesq approximation:

- Navier-Stokes equations

$$\frac{\partial u_i}{\partial t}+\frac{\partial u_k u_i}{\partial x_k}=-\frac{1}{\rho_0}\frac{\partial \pi^\star}{\partial x_i}-\epsilon_{ijk}f_j u_k+\epsilon_{i3k}f_3 u_{g,k}+g\frac{\theta_V-\langle\theta_V\rangle}{\langle\theta_V\rangle}\delta_{i3}-\frac{\partial}{\partial x_j}\left(\overline{u_i'' u_j''}-\frac{2}{3}e\delta_{ij}\right) \tag{2.1}$$

- First principle of thermodynamics

$$\frac{\partial \theta}{\partial t}=-\frac{\partial u_j\theta}{\partial x_j}-\frac{\partial}{\partial x_j}\left(\overline{u_j''\theta''}\right)-\frac{L_V}{c_p\Pi}\Psi_{q_V} \tag{2.2}$$

- Equation for humidity

$$\frac{\partial q_V}{\partial t}=-\frac{\partial u_j q_V}{\partial x_j}-\frac{\partial}{\partial x_j}\left(\overline{u_j'' q_V''}\right)+\Psi_{q_V} \tag{2.3}$$

- Equation for any passive scalar

$$\frac{\partial s}{\partial t}=-\frac{\partial u_j s}{\partial x_j}-\frac{\partial}{\partial x_j}\left(\overline{u_j'' s''}\right)+\Psi_s \tag{2.4}$$

- Continuity equation

$$\frac{\partial u_k}{\partial x_k}=0 \tag{2.5}$$

Here, angle brackets denote horizontal domain averages, the subscript "0" indicates a surface value, a double prime indicates SGS variables. The overbar indicates filtered quantities and it is omitted for readability, except for the SGS flux terms.

For variables that cannot be explicitly calculated, turbulent closure is realized through the following parameterizations [11]:

- Closure for 2.1

$$\overline{u_i'' u_j''}-\frac{2}{3}e\delta_{ij}=-K_m\left(\frac{\partial u_i}{\partial x_j}+\frac{\partial u_j}{\partial x_i}\right) \tag{2.6}$$

- Closure for 2.2

$$\overline{u_i''\theta''}=-K_h\frac{\partial \theta}{\partial x_i} \tag{2.7}$$

- Closure for 2.3

$$\overline{u_i'' q_V''}=-K_h\frac{\partial q_V}{\partial x_i} \tag{2.8}$$

- Closure for 2.4

$$\overline{u_i'' s''}=-K_h\frac{\partial s}{\partial x_i} \tag{2.9}$$

All the above equations are solved on a discrete grid of sizes Δx, Δy and Δz, with a discrete time step chosen by the user based on Courant–Friedrichs–Lewy (CFL) criterion. In appendix A, we presented more detailed description of all the variables A.1 and parameters A.2 used.

An important feature of the PALM LES model is the possibility of including complex topography. If no overhanging structures are present, which was the case for the study we have performed, any topography is seen as a 2D elevation matrix. Since the whole domain is discretized in rectangular grids, obstacles are approximated by an appropriate number of full grid cells to fit the 2D matrix. A grid cell can either be 100% obstacle or 100% fluid. The obstacles must be fixed (not moving). When using topography, the PALM domain is split into three subdomains described as follows:

1. Grid points in free fluid without adjacent walls, here the standard PALM code is executed.

2. Grid points next to walls, they require extra code for wall fluctuations [9].

3. Grid points within obstacles, they are excluded from calculations.

Within the second subdomain, the obstacles are always located where the respective wall-normal velocity components u, v, and w are null. This guarantees that the impermeability boundary conditions are respected.

If non-cyclic horizontal boundary conditions are used, PALM offers the possibility of generating time-dependent turbulent inflow data by using a turbulence recycling method. This is convenient to realize a realistic turbulent flow when obstacles are present in the domain. In all the simulations of our work we have made use of this feature. Figure 2.1 shows a schematic representation of the turbulence recycling method used in this study.

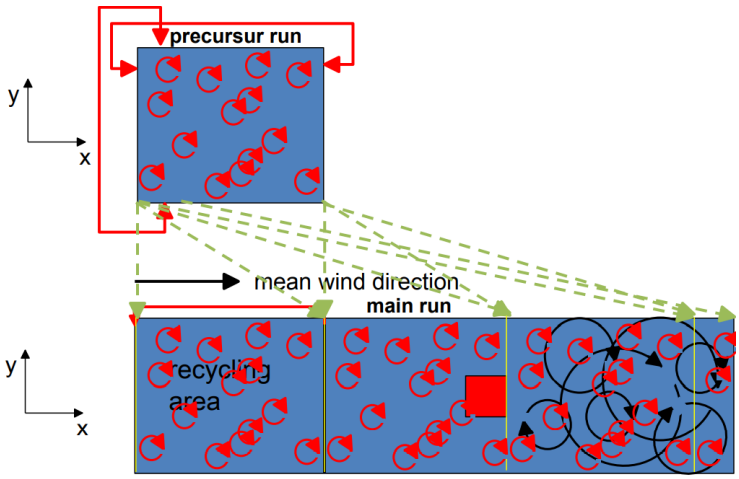

Figure 2.1: Schematic representation of a turbulence recycling. The precursor run is executed on the leftmost square of the domain, the main run involves the precursor run domain and the actual simulation domain. The red rectangle represents a possible topography element. The green lines indicate where the precursor run is mapped. Source: PALM Seminar February 9th 2022, L-3.2: Non-cyclic boundary conditions.

A precursor run is executed in a subset of the domain without topography until turbulence is generated. When the precursor run is finished, data of its last time step is stored on the disk. These data are read by the main simulation that includes topography and

repeatedly mapped in the main spatial domain. The turbulent signal $\phi'(y,z,t)$ is taken from a recycling plane that is located at a fixed distance $x_{recycle}$ from the inlet:

$$\phi'(y,z,t) = \phi(x_{recycle},y,z,t) - \langle\phi\rangle_y(z,t) \tag{2.10}$$

where $\langle\phi\rangle_y(z,t)$ is the line average of a prognostic variable $\phi \in \{u,v,w,\theta,e\}$ along y at $x = x_{recycle}$. $\phi'(y,z)$ is then added to the mean inflow profile $\langle\phi_{inflow}\rangle_y(z)$ at x_{inlet} after each time step. Complete details of the PALM LES model can be found in [9].

2.2 The Gaussian plume model

The Gaussian model is one of the most simple ways for describing the transport of a tracer at local scales. It is widely used for several reasons: it produces results that agree well with experimental data in a vast array of conditions, it is fairly easy to implement and interpret mathematically, and computationally inexpensive.
In this study, we used the Gaussian model presented in [2]. Consider a continuous point source emitting at a rate q, at an effective height H above the ground. Notice that H is higher than the actual source height, this is due to plume rise depending on to the exit velocity of plume from the source, source size at the exit, and the difference between the source temperature and ambient temperature. The average concentration C at a point X,Y,Z (the source is set in the origin) is then given by the formula:

$$C(X,Y,Z) = \frac{q}{2\pi\sigma_Y\sigma_Z U_{eff}} exp\left(\frac{-Y^2}{2\sigma_Y^2}\right)\left[exp\left(\frac{-(Z-H)^2}{2\sigma_Z^2}\right) + exp\left(\frac{-(Z+H)^2}{2\sigma_Z^2}\right)\right] \tag{2.11}$$

where U_{eff} is the uniform effective horizontal wind speed at the effective source height. The coordinate X refers to the plume axis defined based on the mean wind direction. The coordinate Z is for the height above the ground surface, which is assumed to be flat and uniform. The parameters σ_Y and σ_Z are standard deviations of C in the Y and Z direction, respectively. The last term in square brackets accounts for reflection of the tracer from the surface, simulated by considering an image source at the height level $Z = -H$ and assuming no adsorption by the surface. A schematic representation of a Gaussian Plume is presented in figure 2.2. In this study, the parameters σ_Y and σ_Z are parameterized following the formulation of [12]:

$$\sigma_Y = \sigma_v t\left(1+\sqrt{\frac{t}{2T_Y}}\right)^{-1} \quad \sigma_Z = \sigma_w t\left(1+\sqrt{\frac{t}{2T_Z}}\right)^{-1} \tag{2.12}$$

where σ_v and σ_w are the standard deviations of the horizontal and vertical components of the turbulent velocity fluctuations. $t = \frac{X}{U_{eff}}$ is the travel time from origin to X. $T_Y = 200$ s for near surface releases [13], $T_Z = 300$ s for unstable conditions (Obukhov length $L < 0$) [12]. For low wind conditions ($U_{eff} < 1.5$ m/s) the horizontal standard deviation becomes $\sigma'_Y = \sqrt{\sigma_Y^2 + (\sigma_v t)^2}$. In order to obtain effective mean wind speed at effective source height, the mean wind speed at height Z is defined by a power law profile as:

$$U(Z) = U_r\left(\frac{Z}{z_r}\right)^{\alpha} \tag{2.13}$$

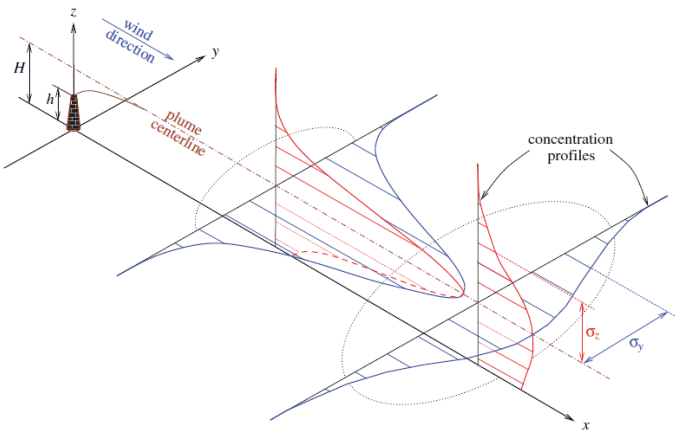

Figure 2.2: A contaminant plume emitted from a continuous point source, with wind direction aligned with the X-axis. Profiles of concentration are given at two downwind locations (vertical in red, horizontal in blue) and the Gaussian shape of the plume cross-sections are shown relative to the plume centerline. Source: [1].

where U_r is the wind speed measured at the reference height z_r and α is obtained as [14]:

$$\alpha = \frac{u_\star \phi_m \left(z_r/L\right)}{kU_r} \tag{2.14}$$

where $u_\star$ is the friction velocity, $k = 0.4$ is the von Karman constant and ϕ_m is the stability function of momentum. For our study, we have used the parameterization of ϕ_m from [15]:

$$\phi_m \left(Z/L\right) = \left(1 - 16Z/L\right)^{-1/4} \tag{2.15}$$

Chapter 3

INDUSTRIAL AND LANDFILL SITES UNDER STUDY

3.1 TADI-2019 campaign

Site description and meteorological conditions

Between 2 and 10 October 2019, the TRACE team participated to an experiment involving several controlled releases of CH_4. The campaign was conducted at TotalEnergie's controlled release test TADI, in Lacq (latitude: 43.413°N, longitude: 0.642°W). The TADI site is a predominantly flat area of about 200 m × 200 m, containing small roughness elements such as decommissioned oil and gas equipment. Several controlled releases of CH_4 were performed in an area of 40 m × 50 m, ATEX zone as depicted in figure 3.1. We have used here data from one of the releases performed between 08:13:00 and 09:11:00 UTC on 2-10-2019. During that release the wind speed was between 2 m/s and 4 m/s from south west and the atmospheric condition was unstable. Figure 3.1 shows a representation of the site and experimental setup. Details of the experimental setup, instruments, and different types of measurements is given in [2].

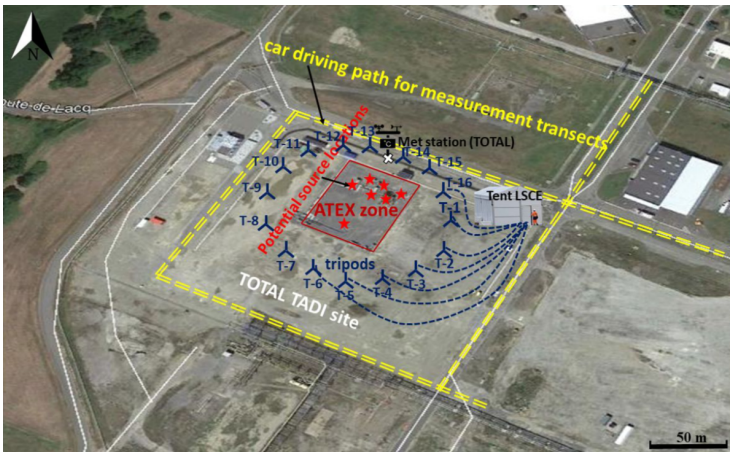

Figure 3.1: Schematic representation of the TADI site. The rectangle in red shows the zone used for the controlled releases (ATEX zone), the red stars are possible sources. The yellow paths correspond to the location of car measurements. The tripods for fixed measurements are schematized in blue. Source: [2].

Measurement framework and available data

In the controlled release studied in this study, methane was released with an emission rate $Q = 10$ g s^{-1} at a height of 0.96 m, and it corresponds to the star at the bottom of the release zone. The meteorological data was provided by TotalEnergie through a Metek 3D Sonic anemometer installed at a 5 m height in the location shown in figure 3.1. The instrument provided 1 min averages of wind direction (W_{Dir}), wind speed (W_s), temperature (T), Monin-Oukhov stability parameter ($1/L$), surface friction velocity ($u_\star$), and standard deviation of each component of the wind velocity fluctuations (σ_u, σ_v, σ_w).

During the release, fixed-point measurements were performed at the fixed tripods assigned with numbers 1, 2, 3, 4, 15, 16 (Figure 3.1). The air intake was placed at a height of 3.50 m above the ground for each tripod. We used high precision gas analyzers to measure the methane mole fraction at the fixed tripods. The gas analyzers consisted of four Picarro G2401 cavity ring down spectrometers (CRDS) analyzers that measure CH_4, CO_2, CO and H_2O, two Picarro G2201-i isotopic CRDS analyzers for $^{13}CH_4$, $^{12}CH_4$, $^{13}CO_2$, $^{12}CO_2$ and H_2O, and one ABB Micro-portable Greenhouse Gas Analyzer (MGGA) measuring CO_2, CH_4 and H_2O. Each gas analyzer measured H_2O mole fraction to correct the water vapour effect and provide mole fraction in dry air. Continuous methane mole fraction measurement were made at approximately 1 Hz frequency. Mobile concentration measurements were performed simultaneously with the fixed-point measurements through a Picarro G2210-i analyzer mounted on a vehicle that was driven along the roads in yellow. The air inlet of the mobile instrument was at 2 m above the ground for the entire experiment and GPS location of the car was stored.

3.2 Landfill site

Site description and measurement campaign

The case study presented here is based on a mobile measurements campaign conducted at a landfill site in Amailloux, west France, operated by SUEZ that is also used for biogas collection. The landfill has a vast range of potential emission sources that vary from pipe junctions to holes in the waste sheet cover heterogeneously spread in the domain. The surrounding region of the landfill site is characterized by a predominantly flat orography. The topography of the landfill is complex and its elevation varies approximately between 199 and 236 m a.s.l. over an area of roughly 800 m $\times$ 800 m. The mobile measurements considered here, were performed on the three roads downwind from the landfill and inside the landfill itself during daytime on 24-03-2021. The total length of the road over which the plumes were measured is about 900 m, and the distance from the sources is on the order of 400 m. The atmospheric conditions during the campaign were characterized by mild wind speeds coming from south west. A map of the site, including the measurement roads is shown in figure 3.2.

Measurement framework and available data

The meteorological data used in this study was recorded by a 3D Sonic Anemometer at 20 Hz. The instrument was located at 6.2 m above the ground approximately at the centre of the landfill, in a place that could be the most representative for the overall meteorological conditions. The quantities recorded where: time t, (u, v, w) components of the velocity, speed of sound SOS, temperature T, wind direction W_{Dir} and wind speed W_s.

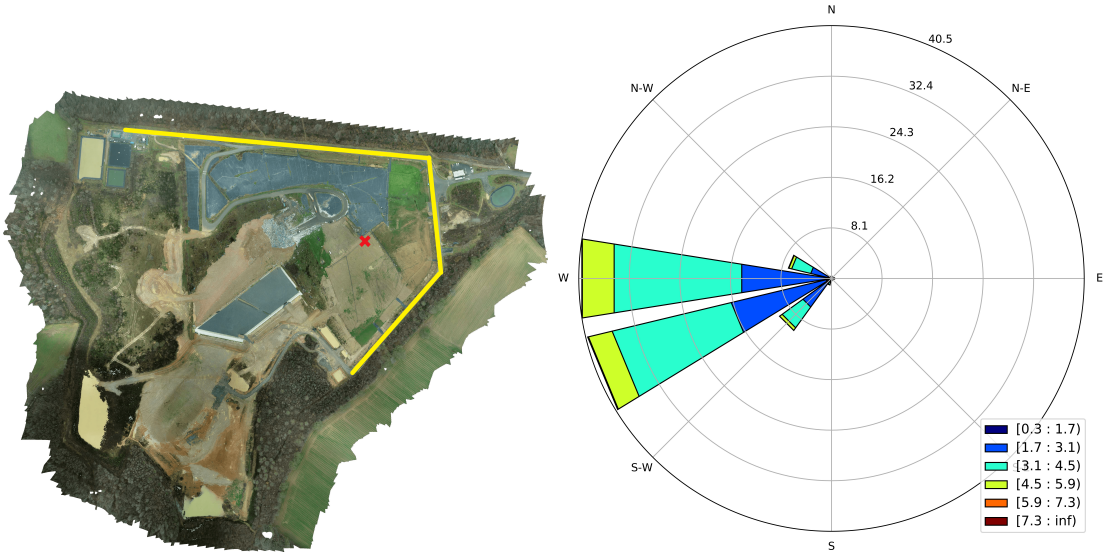

Figure 3.2: Left: Map of the landfill provided by SUEZ. The roads over which the mobile measurements are performed are depicted in yellow. The red cross in the center of the landfill represents the 3D Sonic Anemometer used for meteorological data. Source: drone mapping company Propeller. Right: Wind rose on 24-03-2021.

The CH_4 mole fraction data used in this work was measured by a LI-COR sensor mounted on a car at a sampling frequency of 1 Hz. With this analyzer, coupled with a GPS, wet and dry CH_4 mole fractions, and positions and time of measurement were recorded. The height of the inlet of the measurement device was at about 2 m above the ground for the entire measurement. The time of recording was corrected by a factor in order to take into account the delay between the GPS location and the actual measurement (i.e. time taken by air sampled at inlet to reach the analyzer).

Chapter 4

LARGE EDDY SIMULATIONS

4.1 Boundary conditions and Numerical methods

Table C.1 summarizes all the boundary conditions used in the LES simulations. For flow field simulations, we used a turbulence recycling method in which the precursor run is performed with cyclic boundary conditions on both Y and X axis (these axes refer to the horizontal domain shown in figure 4.1). The boundary conditions for the u and v components of the velocity were set as "no slip" condition at the bottom, i.e. $u = v = 0$ m/s, and "Dirichlet" at the top, with a value depending on the chosen geostrophic wind. The main run is then performed with different boundary conditions on the two horizontal axes. The Y axis, where the magnitude of the respective wind component is lower, had still cyclic boundary conditions. This choice, even if not completely realistic, was done because the PALM code does not allow to have non cyclic boundary conditions on more than one axis. As we will see, this may cause some problems in the simulated v component of the wind field. The boundary conditions for the X axis were "Dirichlet" at the inflow defined from the precursor run and "Neumann" at the outflow.

For the perturbation pressure $p^\star$, the bottom boundary condition was "Neumann", while the top one was "Dirichlet" (in the last grid on the Z axis we have set $p^\star = 0.0$ hPa). For the potential temperature, we used "Neumann" at the bottom, while the top value was calculated within the model through a gradient of 1.0 K/100 m starting from $z = 800$ m.

For plume simulations by considering methane as a passive tracer, we set "Dirichlet" at the inflow boundary and "Neumann" at the outflow boundary. Top and bottom boundary conditions were set to "Neumann". Lateral boundaries were also set to "Neumann".

The time integration method used for the prognostic variables was a third order Runge-Kutta scheme. For momentum and scalar advection, we have used the 5^{th} order upwind scheme of Wicker and Skamarock [16]. For pressure solver, we have used the multigrid scheme by [17] because it does not require cyclic lateral boundary conditions. For fast Fourier transform method (FFT), we have chosen to use the Singleton algorithm [18]. This method is slower than the default one built in PALM, but it is less restricting and can be used in almost any configuration. In every simulation we have set a Rayleigh damping factor of 0.02 starting from $z = 500$ m to speed up convergence of the prognostic variables to their basic states, defined by the initial values chosen by the user. Random disturbances to the flow with an energy limit of 0.01 m^2/s^2 (in PALM the unit of mass is set to 1) were included in the simulation.

4.2 LES simulation setup specific to the campaigns

For the simulation of the TADI-2019 experiment, the tracer source was simulated as a point source, because the release area, being a pipe, was smaller than the size of the grid size of our simulation. For the landfill simulation, we had to modify the source code in order to simulate custom area sources, as it will be explained in section 4.3.

4.2.1 Lacq site

We defined a 3D domain of (512 m × 256 m × 1506 m) with (256 × 128 × 192) grid points in (x, y, z) directions, respectively. The precursor run covered the left half of the domain. The horizontal resolution was set to 2 m, while the vertical resolution was of 2 m only for the first 150 m. After the first 150 m, the resolution follows a geometrical series with stretching factor of 1.025. The stretching factor was chosen in order to be able to reach the top z level sufficiently high to simulate the boundary layer with an affordable computational cost. In choosing this parameter, we have also checked that the condition $\sqrt[3]{dxdydz} < 2.7dx \ \wedge \ \sqrt[3]{dxdydz} < 2.7dy$ was always verified, this is necessary to obtain realistic simulations as explained in [9]. Since the topography of the Lacq site is flat and homogeneous, we have not included a topography file in this case. As roughness we have chosen a constant overall value of 0.03 m, suitable for this type of terrain as described in [19]. The simulation was set up using average values measured by the 3D Sonic Anemometer between 08:13:00 and 09:11:00 UTC, which is the time window of the release that we are trying to model. The average temperature $T = 290.08$ K has been set in the model as a constant surface potential temperature. The average wind components used were $u = 2.75$ m/s and $v = 0.12$ m/s. Moreover, we have used a constant sensible surface heat flux of 0.026 K m/s, calculated from 3D sonic data using the eddy covariance method. We performed two different tests by forcing the wind speed and direction through two different methods. The first one consisted in the use of surface geostrophic winds and the second one in setting a wind profile in the first 100 m of the vertical domain. The wind profile for u and v have been calculated using 2.13. This last setting has not been used with the complex terrain of the landfill, because in that case it is ambiguous to define a profile in the first 40 m of the domain. As source, we have added a constant point source of rate 10 g s^{-1} at the actual location defined in the Lacq experiment.

Throughout the simulation, we have collected 1 min averaged CH_4 concentration on all the car positions, 1 Hz concentration data at the positions corresponding to the tripods active during the controlled release, wind direction and wind speed at 1 Hz at the actual location of the 3D sonic anemometer.

The precursor run is simulated for 40000 s in "virtual time", to be sure to have a fully converged result. The main run is then simulated for another 40000 s. After that, the final simulation has been restarted from the last time step by adding a point source release for 3600 s. The precursor run simulation lasted for 20.5 h on 8 cores, the main run for 25 h on 16 cores and the simulation of the release for 3.5 h on 8 cores.

4.2.2 Landfill site

The setup used here is similar to the one used for the previous case, with few changes in the parameters and including the topography of the landfill. The LES was performed in a three-dimensional domain of 2.560 × 1.280 × 2.051 km with 256 × 128 × 128 grids in x, y and z directions respectively. This results in a uniform horizontal resolution of 10

m, while the vertical direction is resolved on a stretched grid with a 2 m resolution in the first 150 m of the domain. The stretching factor chosen here was of 1.085. In table 4.1 we summarize the meteorological data used for both setups. The meteorological parameters set were: $T = 286.03$ K, $u = 2.6$ m/s, $v = 1.7$ m/s and sensible heat flux of 0.074 K m/s. In order to use the landfill topography in our simulation, we have adapted the topography map provided by SUEZ to our domain. Since we have trees on the edge of the landfill elevation map, as one can spot by the left part of figure 3.1, we have started by removing them from the data. We have done that because no precise information on the location of the trees was provided and if we had left them in the topography map, the simulation would have seen them as hard topography elements, while, instead, to simulate the flow on a forest one should use the "canopy module" implemented in PALM. After that, we have created a rectangular domain, as required by the PALM code, by smoothly extending the topography map taking values from the edges. The extension is more pronounced in the left side of the map because we needed to create a "buffer zone" used for the precursor run.

Using the topography file, we have also created a roughness matrix that associates each point in the topography to its roughness. The roughness has been evaluated using the geometrical approach described in [20], where it is taken as the largest inter-cell difference of a central pixel and its surrounding cell. This value is then divided by a factor 10 following [21]. Since the topography data was provided with an extremely high resolution (approximately 0.1 $\times$ 0.1 m), we have resampled it by taking averages over boxes of 10 $\times$ 10 m, in order to obtain a topography and roughness matrix of shape 128 $\times$ 256 corresponding to LES model setup. We have considered seven potential area sources for methane plume simulations. The spatial distribution of these sources is obtained from an analysis of a "sniffing campaign" conducted in a previous study. For the description of a recent "sniffing campaign", we refer to appendix B. See figure 4.1 for a summary on our topography treatment.

The precursor and main run were simulated for the same amount of "virtual time" as before. The final main simulation is restarted from the last time step adding each of the area sources and performed for a time for 5400 s. The first 3600 s served to let the tracer disperse (the source is considered constant in time, therefore we have to reach a sort of "stationary state" also in the simulation), the last 1800 s have been used to collect concentration data analogous to the one collected by the car measurements. Throughout the simulation, we have also collected W_{Dir} and W_s at 1 Hz at the same position of the 3D Sonic Anemometer. The simulation lasted 19 h for the precursor run, 34 h for the main run and 6.5 h for each of the area sources. Each simulation was run on 8 cores.

Table 4.1: Summary on meteorological conditions used.

Variable	Lacq	Landfill
T	290.08 K	286.03 K
u	2.75 m/s	2.60 m/s
v	0.12 m/s	1.70 m/s
sensible heatflux	0.026 K m/s	0.074 K m/s

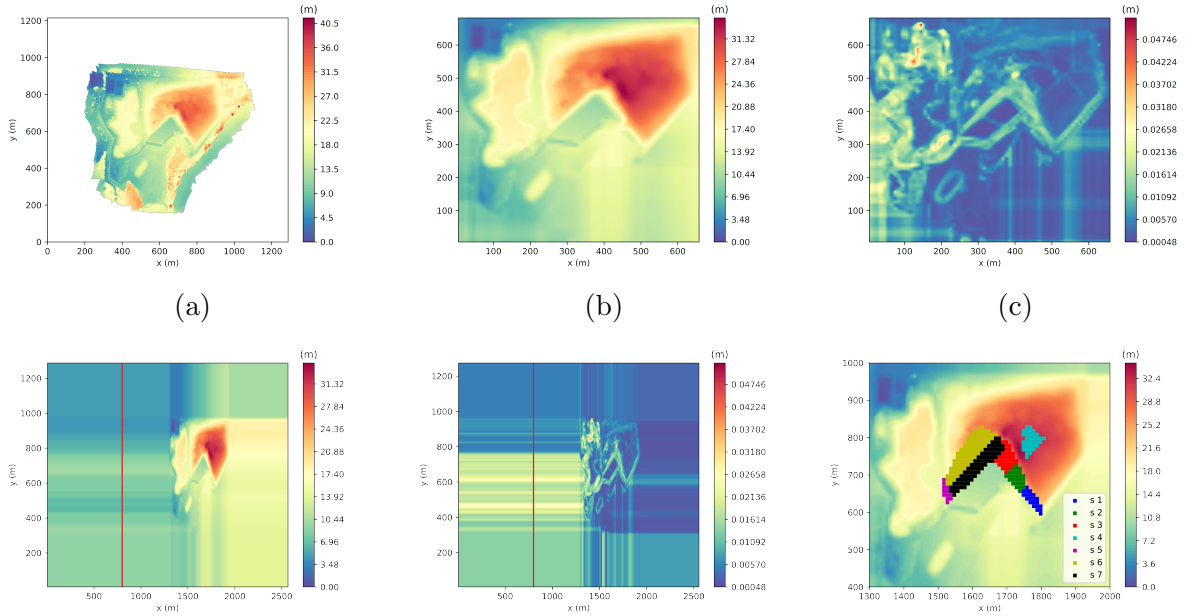

Figure 4.1: 4.1a: Original topography provided by SUEZ on 27-01-2021, the shape is irregular and it contains trees on the edges. Source: drone mapping company Propeller. 4.1b: coarse grained and and smoothly reshaped topography without trees. 4.1c: coarse grained roughness evaluated through a geometrical approach. 4.1d and 4.1e: extended topography and roughness, the red line indicates the limit for the precursor run. 4.1f: schematic representation of the seven area sources considered.

4.3 Code implementation for complex area sources

The PALM default code allows to set scalar sources as Eulerian fields, but only for surface area sources that cover the whole top face of complex topography or the whole flat terrain considered in a simulation. It does not allow by default the use of area sources of any desired shape or dimension on any place of the domain. In a previous implementation of the LSCE SATINV group, the source code was modified in order to be able to set point sources or rectangular area sources anywhere in the domain. In the course of this study, the code was further modified in order to allow the setting of area sources of any desired shape anywhere in the domain. With our modification, the information on the location of the sources is assimilated through a static NetCDF file. The file, apart from information on topography and roughness previously discussed, contains a further matrix of the same size of the domain grid that specifies the flux emitted at each grid point. In this way the program has information on where to add flux terms and on where to suppress them in equation 2.4. We have tested the new implementation on simple cases that could be covered also by the default one and obtained a perfect match.

4.4 Convergence tests

In order to have reliable results, we have tested the convergence of the LES simulations with respect to many aspects. For the first test of convergence with respect to the simulation time, we analyzed the time series of four different quantities: the total energy of

the flow averaged on the grid, the maximum of u, v and w components of the velocity. Convergence is reached when each of those quantities reaches a plateau. In figure 4.2, we present an example of the convergence plots obtained for the precursor run of the landfill simulation. As one can see from the plot of the energy time series and from the plot of the maximum u, v and w wind components time series, a plateau is already reached after about 5000 s. This means that the run time of 40000 s, that we have chosen for our simulation, is enough to obtain a reliable wind flow. The analogous plots for the other measurement time windows and for the Lacq case are also conducted (not shown) and the results are very similar to that we obtained for landfill simulations.

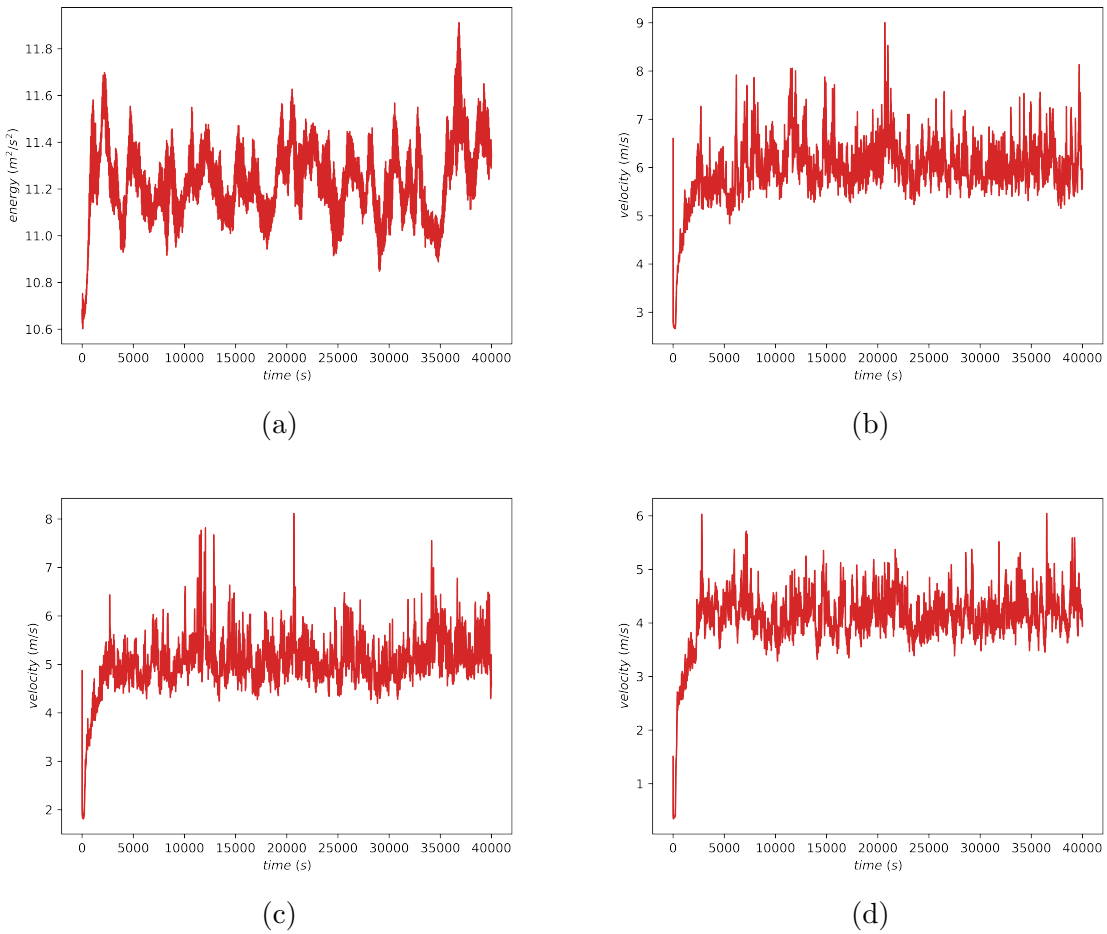

Figure 4.2: 4.2a: time series of total energy averaged on the grid. 4.2b, 4.2c, 4.2d: time series of maximum u, v and w components of the velocity.

The second test that we have performed was relative to the grid size of the spatial discretization. The choice of the horizontal grid size of 10 m $\times$ 10 m was mostly driven by our limited computational resources. Nevertheless, we have checked whether such a size was small enough to perform a real LES, which happens if we are not neglecting eddies that transport a large energy. To this end, we have analyzed four different quantities: the difference between the time series of the resolved scale turbulent kinetic energy (RS TKE) and the sub grid scale turbulent kinetic energy (SGS TKE), the spectral decomposition of the u, v and w velocity components recorded at a z level of 70 m along the y axis. The results are shown in figure 4.3, the plots are corresponding to the main run of the simulation of the landfill case. The fact that the SGS TKE is one order of magnitude lower than

the RS TKE suggests that the simulation is neglecting only secondary eddies, therefore the grid size is small enough. This is also confirmed by the spectral decomposition of u, v, and w. All the spectra are peaked at low values of wave numbers. Thus the largest eddies contain the highest variance. With these arguments we can demonstrate that our choice of the grid is sufficient to represent the flow from an energetic point of view, but we cannot ensure that the grid is small enough to contain all the relevant details of the topography and of the simulated CH_4 plumes. Similar results are obtained for TADI-2019 simulations (not shown). To expand this work, one would need to study the variation of the plume statistics with the change of the grid size, this kind of analysis has not been performed at this stage.

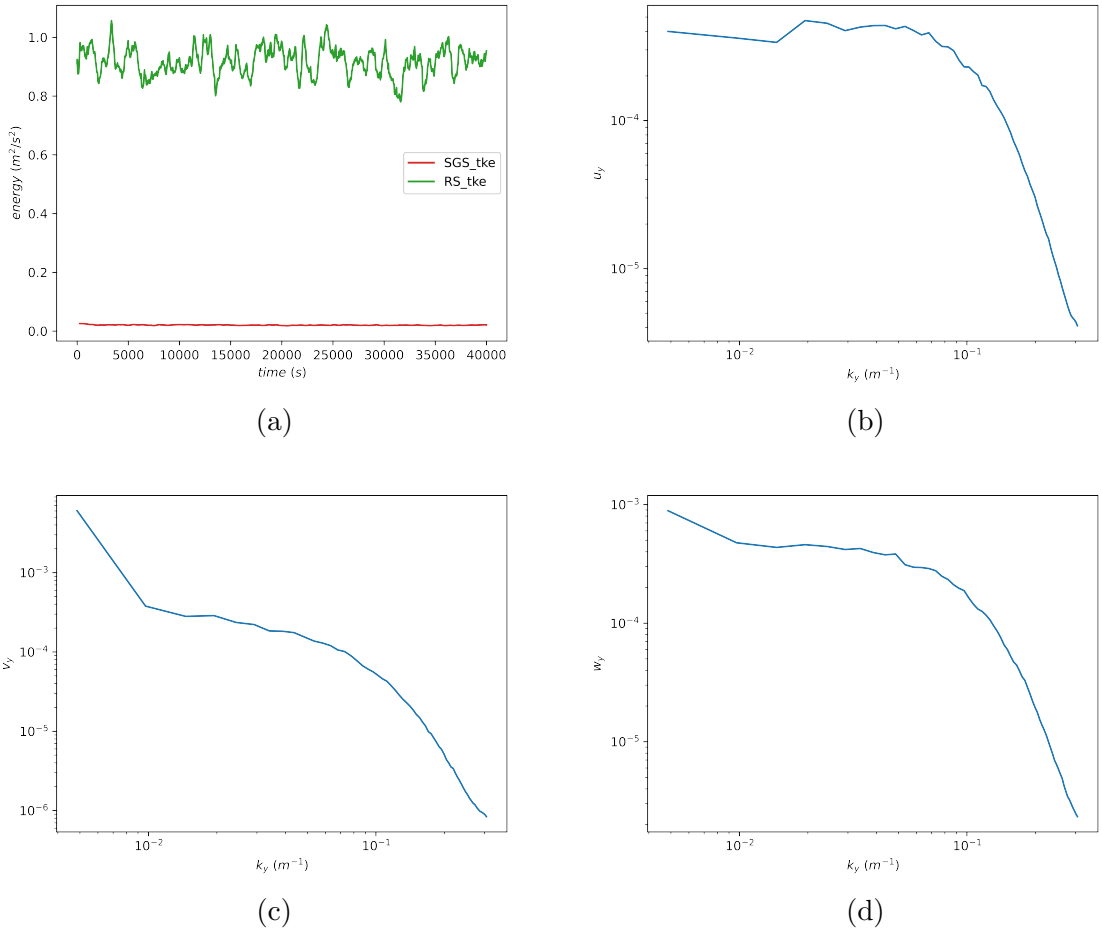

(a) (b)

(c) (d)

Figure 4.3: 4.3a: time series of SGS vs RS TKE. 4.3b, 4.3c, 4.3d: spectral decomposition of u, v and w components of the velocity along the y axis. The values are relative to the last time step of the main run of the landfill simulation. The spectral densities are dimensionless (otherwise they would be m^3/s^2) because in PALM they are normalized to the variance at the corresponding height level and additionally multiplied by the wave number.

The last test that we have performed was in order to asses whether the size of the domain was large enough to catch all the relevant structures of the flow. This kind of test was more qualitative and it consisted in visually checking if all the patterns appearing in the flow were well contained by the horizontal domain. To this end, we have analyzed the behaviour of the w component of the velocity and of the potential temperature θ at two

different z levels over the whole horizontal domain. From our results, shown in figure 4.4, one can see that all the structures formed by the flow are well contained by the horizontal domain. Therefore our choice of the horizontal domain is appropriate.

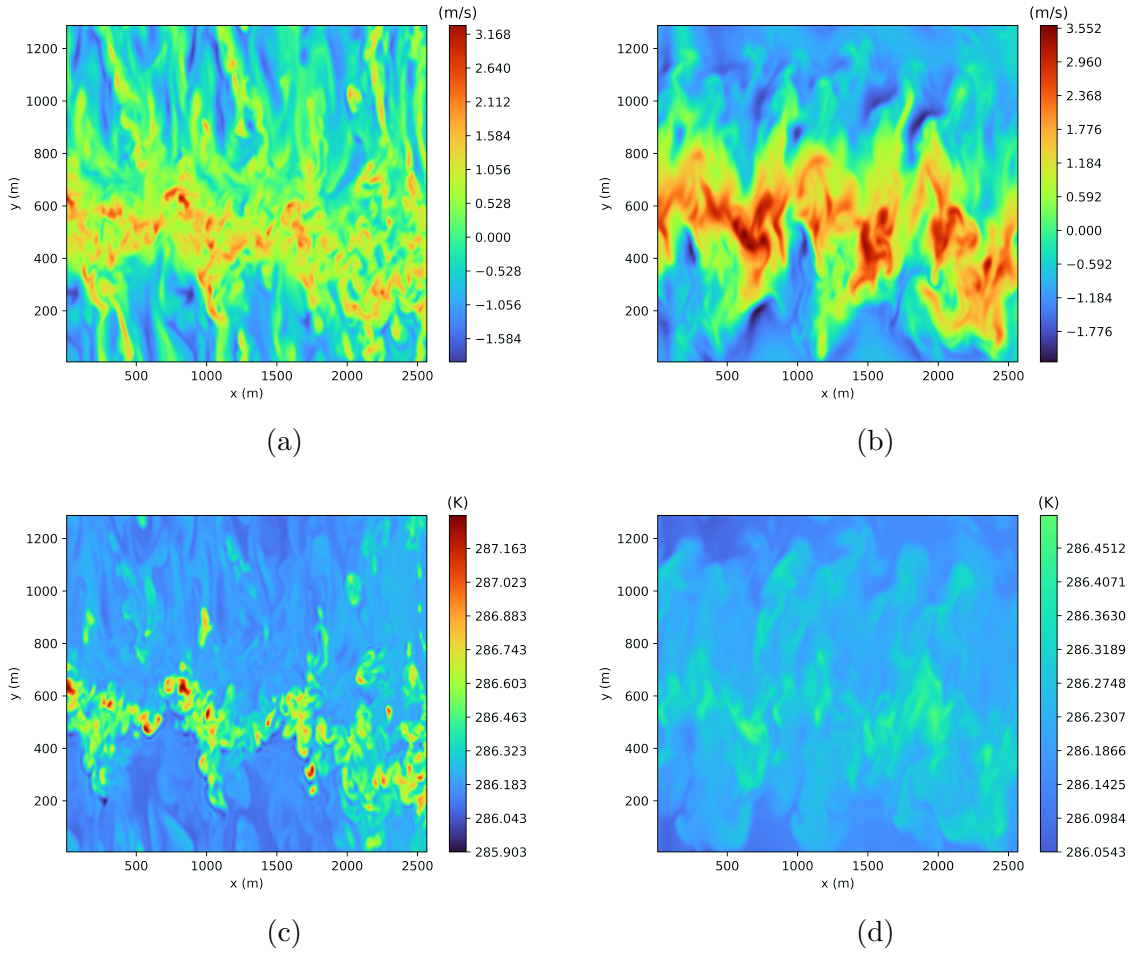

Figure 4.4: 4.4a and 4.4b: colormap of w component of the velocity at $z = 100$ m and $z = 586$ m respectively. 4.4c and 4.4d: colormap of θ at $z = 100$ m and $z = 586$ m respectively. For both w and θ we have set the same scale on the colormap at the two different z levels in order to provide also a comparison of the behaviour of the flow at different altitudes.

Chapter 5

RESULTS AND DISCUSSION

5.1 Evaluation of LES with TADI-2019 experiment

Since we have methane mole fraction measurements from a point source release with known rate and location in TADI-2019 experiment, we use them to evaluate the performance of our LES setup for simulating emission plumes. Here in fact, the misfits between simulations and observations are only due to model error. Nevertheless, it is important to bear in mind that the plume emission that we are trying to simulate at the landfill differs from the one at TADI-2019 by scale, meteorological conditions and topography. It is important to specify that, in both the models that we have used, the methane mole fractions that we are simulating is actually the methane enhancement above the background due to the presence of a source. Therefore, in all the comparison with observations, we have first removed the background by subtracting the minimum value of the methane mole fractions measurement time series.

We perform the first comparison between the simulated and measured meteorological conditions. The two variables that we will analyze are the wind speed W_s and the wind direction W_{Dir}, for both the wind forcings described in section 4.2.1. Our results are shown in figure 5.1.

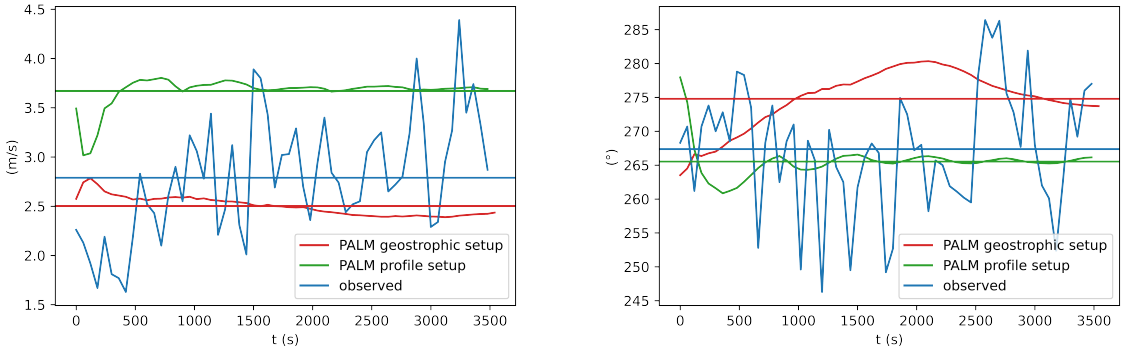

(a) (b)

Figure 5.1: 5.1a: A comparison between the wind speed obtained with the two different wind setups (red: geostrophic wind forcing, green: wind profile forcing) and the observed wind speed (blue). 5.1b: comparison between the wind direction obtained with the two different wind setups and the observation. The horizontal solid lines represent the respective average values.

These figures show that the "profile" and the "geostrophic" setup yield very different

wind fields. The geostrophic forcing is more accurate in simulating the wind speed, producing a lower bias than the profile setting. But when it comes to the wind direction, we observe the opposite behaviour, the profile forcing yields a wind almost perfectly aligned to the observed one, while the geostrophic setup produces a bias of about 7°. In both simulations, the standard deviations obtained are much lower than the observed ones: for W_s we obtain $\sigma_{obs} = 0.59$ m/s, $\sigma_{pro} = 0.15$ m/s and $\sigma_{geo} = 0.10$ m/s for the observation, the geostrophic setup and the profile setup respectively; for W_{Dir} we have $\sigma_{obs} = 9.0$ °, $\sigma_{pro} = 2.4$ ° and $\sigma_{geo} = 4.2$ °. In this case it is not possible to perform a proper comparison between the speed of variation of the wind fields since the measured winds are sampled only every 60 s. Nevertheless, it is easy to see from the plot that the model is much smoother than the observation.

The next step in our analysis is to compare the time series of methane mole fraction measurements from the fixed tripods with the LES simulations. Using a LES we can both produce instantaneous data and average data. Our results are shown in 5.2.

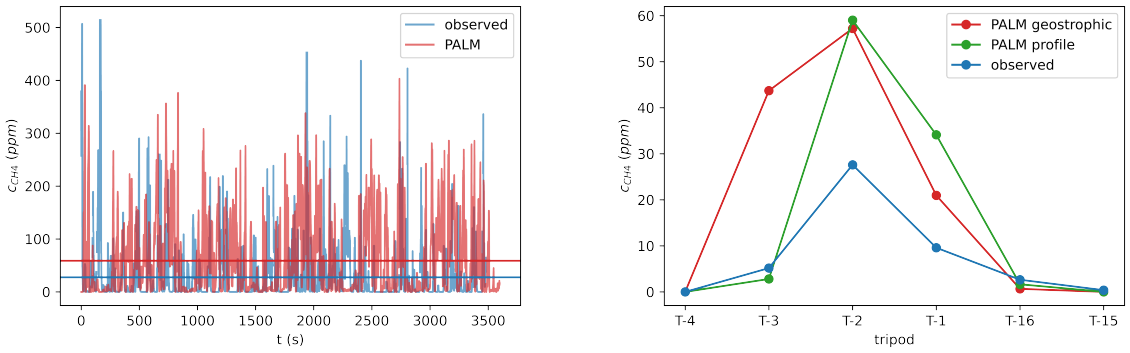

(a) (b)

Figure 5.2: 5.2a: An example of the CH_4 mole fractions time series from a fixed tripod-2 with the profile setup (red) and the observation (blue). The horizontal lines represent average values. 5.2b: average concentrations for each tripod for observation (blue), geostrophic setup (red) and profile setup (green).

As one can observe especially from figure 5.2b, the overall behaviour is captured by the LES simulations and the order of magnitudes of the average values from both simulation setups is similar with the observations. The results with the LES simulations with the wind profile, has a slightly better agreement with the observation compared to the one obtained from the geostrophic wind setup. This means that a having a large bias in the wind speed and a low bias in the wind direction leads to better results than the opposite case. In other words, in this case, the wind direction is more relevant than the wind speed magnitude for the production of a simulated plume at local-scale when the distance from the measurement location to the source is small. The main difference between the simulated plume with the profile setup and the real one is that in the simulation we obtain a narrower plume. This is why on tripod 2, where the averaged CH_4 mole fractions has its peak, we observe a higher mole fraction from the simulation with respect to the observations. This behaviour of the modelled plumes is also observed from the Gaussian model [2]. This is mainly caused by the bias in W_s and by the fact that the variability of the simulated wind is lower than that of the real one. Taking inspiration from [2], we have tried to quantify the model error when simulating the fixed point measurements

by calculating the root mean square error (RMSE) between observation and model and normalizing it by the variance of the observed concentration across all the tripods. This RMSE refers to the average data of figure 5.2b. We have obtained a normalized RMSE of 214% for the geostrophic setup and of 170% for the profile setup. With the Gaussian model used in [2], the error obtained was on the order of ≈ 100 %. In that study though the wind had been binned by wind directions, while here we have used only an average overall wind. Therefore, considering how rough it is our model at this stage, the overall result is promising.

Since the profile setup has a better performance, in the second part of the analysis with mobile measurements, we will present only the results obtained with this setting. To this end, we have collected all the car positions and we have used them to produce "simulated transects". The best results for comparison are obtained when taking an average over all times of the plumes produced in the simulation. Our results are shown figure 5.3.

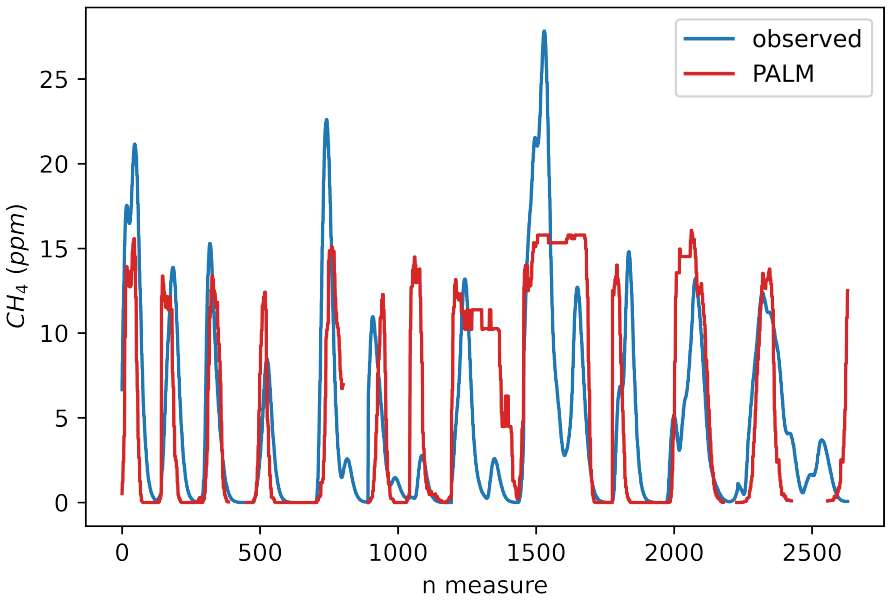

Figure 5.3: Observed (blue) and simulated (red) car transects. In this figure we use an average over all times to produce the simulated transects. The small gaps that are present in the simulated transects are relative to places covered by the car, but not present in our domain.

In order to quantify the accuracy of the model, we have calculated the average of the normalized absolute error over all the transects. The average normalized absolute error is obtained with the following formula taken from [2] $err_{abs} = \langle abs\left(\frac{A_i^{obs} - A_i^{sim}}{A_i^{obs}}\right)\rangle$, where A_i^{obs} and A_i^{sim} are the observed and simulated areas under each peak i respectively. We have obtained a value of $err_{abs} \approx 30$ % for the overall average transects. This result was obtained considering only concentration values larger than 1 ppm in order to avoid a numerical "infinite" in the normalization. The results for the Gaussian model obtained in [2] are of an error of 50%.

5.2 LES performance for landfill site

For the landfill site, we do not have knowledge of the actual emission rate and of its spatial distribution within the landfill for comparison of the LES simulated methane plumes with the observations. So, we estimated the total landfill methane emissions using the simulated methane plumes from LES model in a simple atmospheric inversion approach. Then, we compared this estimated emissions using LES with the one obtained from the inversion using the Gaussian plume model. We investigated the performance of LES simulations of wind field by comparing it with the wind data measured at one meteorological station.

5.2.1 Performance evaluation of LES wind field with the observations

Figure 5.4 shows a comparisons of simulated and observed W_s and W_{Dir}.

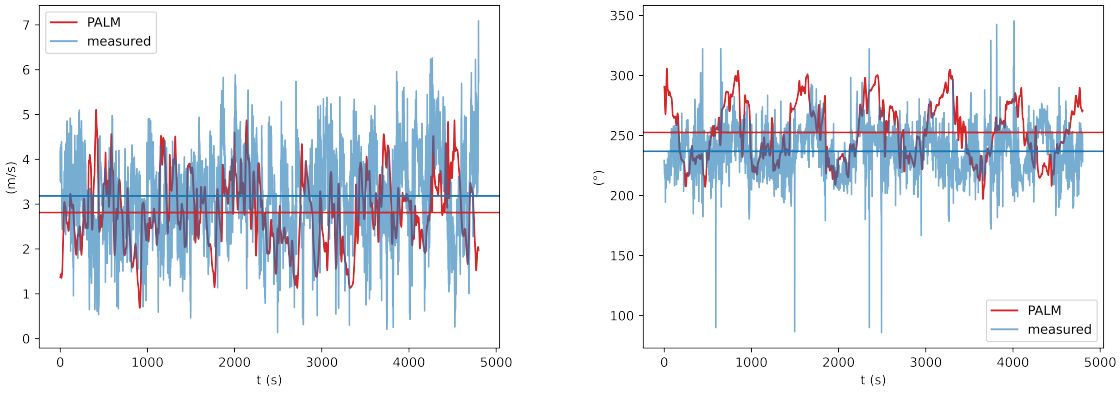

(a) (b)

Figure 5.4: 5.1a: confront between simulated and measured wind speed at the landfill. 5.4b: confront between simulated and measured wind direction at the landfill.

In this case we have only used a geostrophic wind forcing because, with a complex topography, the concept of wind profile becomes ill-defined for low z values. The values of simulated and observed wind speed are very close, on average, with a small underestimation in the simulation. The standard deviation of W_s is higher in the observation than in the simulation: $\sigma_{obs} = 0.98$ m/s, $\sigma_{sim} = 0.81$ m/s for observation and simulation respectively. For W_{Dir}, instead, we have $\sigma_{obs} = 18°$ and $\sigma_{sim} = 24°$. The value of the averaged simulated wind direction differs by about 10° from the observed one. This bias summed to the fact that the measurement itself can be a little biased (see appendix B) may cause some uncertainty in our estimate. By looking closely at figure 5.4a, we observe a sort of periodic behaviour in the simulated wind direction. At first it could appear that this is due to a non completely converged simulation, but, as we have seen in chapter 4, convergence is definitely reached in 40000 s of run. Therefore, the periodic behaviour is most likely due to the cyclic boundary conditions that we have imposed on the Y axis. Hence, this problem could be intrinsic to the model itself and can be solved only by changing the source code by allowing non cyclic boundary conditions on both axes.

Since in this case we have high frequency measurements (1 Hz), we can also determine if the speed of variation of the simulated wind field is well described by the simulation.

To do that, we have performed a spectral decomposition of the signal for both W_s and W_{Dir} and calculated the power spectral density for both time series. This quantity should give an indication on the speed of variation. Our results are presented in figure 5.5.

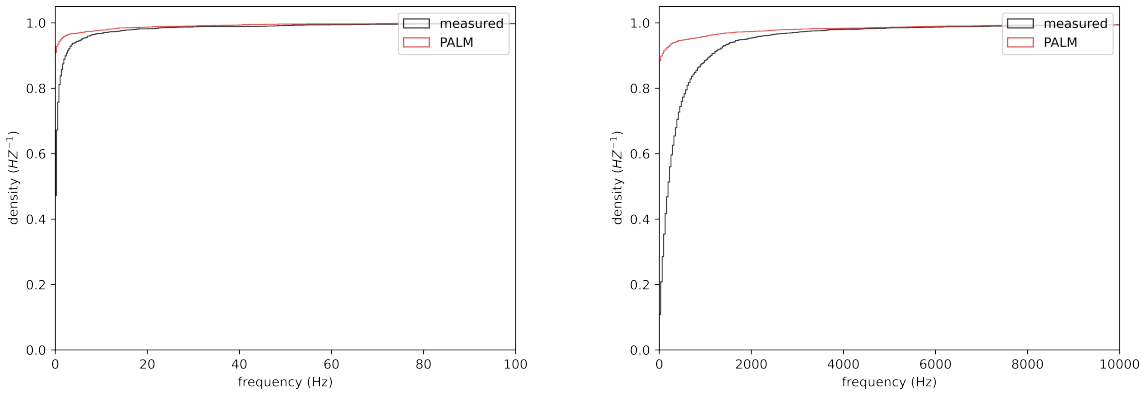

(a) (b)

Figure 5.5: 5.5b: cumulative power spectral density of time series of simulated (red) and observed (black) wind speed. 5.5b: cumulative power spectral density of simulated and measured wind direction.

As one can see both from figure 5.5a and 5.5b, the power spectral density of the simulated wind speed and direction has more components at low frequencies with respect to the observed data. This means that our simulations have produced a "smoother" wind field that varies less rapidly than the observed one. This bias could be corrected in future studies by adding more intense random disturbances to the flow.

5.2.2 Quantification of landfill methane emission

The last part of our analysis consists in the estimation of the methane emission rate from each of the seven area sources considered. Our main assumption is that, the measured concentration depends linearly on the emission rate. Moreover, when considering multiple sources, the measured concentration at a location is the linear contribution of the concentration from all the sources. Consider the row vector $\boldsymbol{c_o}$ that stores all the average concentrations observed in each position during a mobile sampling. For any possible source, we can perform a simulation, considering a source rate normalized to 1 Kg/s, and produce an analogous vector $\boldsymbol{c_i}$ that stores the normalized contribution of source i to the total concentration in each position. Let us denote $\underline{\boldsymbol{A}}$ the matrix obtained combining all the row vectors $\boldsymbol{c_i}$ and $\boldsymbol{q}$ the row vector containing the weight of emission rate of each area source. The matrix product $\boldsymbol{q} \cdot \underline{\boldsymbol{A}}$ should give us the modelled total concentration at each measurement position $\boldsymbol{c_m}(\boldsymbol{q})$. Since $\boldsymbol{q}$ is actually what we want to estimate, we can build the cost function $J(\boldsymbol{q}) = \| \boldsymbol{c_o} - \boldsymbol{c_m}(\boldsymbol{q}) \|^2$. By minimizing $J(\boldsymbol{q})$ with respect to each component of $\boldsymbol{q}$ we obtain the estimated emission rates for each source. This is essentially an inversion based on a least square regression. We have calculated $\boldsymbol{c_m}$ both with the Gaussian and the PALM model, the results for each emission rate are summarized in table 5.1 and figure 5.6.

The total landfill methane emission using LES model is 2285 Kg/d which is higher than the 1457 Kg/d estimated using Gaussian model (Table 5.1). There is a good match

between the two simulations with respect to source 6 and to the total emissions. The Gaussian model though predicts small emission rates for source 1 and 2. Such rates are not obtained when using the PALM model. On the other hand, the PALM model predicts emissions from source 4, while with the Gaussian we obtain no emissions there. The fact that with both methods we find the same order of magnitude for the total emission rate suggests that, at this stage, the impact of the model on the emission outcome is not strong. Nevertheless, some adjustments still need to be done to the LES to obtain more reliable results. The primary source is predicted to have the same order of magnitude by both models because, being at the top of the topography, is less influenced by that. The differences in the secondary sources that we find between the two models are probably due to the complex topography, which is indeed only took into account by the PALM model. With neither of the two models we are able to explain the right tail of the average methane mole fractions in figure 5.6b, this could be due to a bias in the wind direction or also to a missing area source in our model.

Table 5.1: Emissions from each area source with Gaussian and PALM model.

Estimated emissions		
Source	PALM	Gaussian
1	0 Kg/d	10 Kg/d
2	0 Kg/d	193 Kg/d
3	0 Kg/d	0 Kg/d
4	130 Kg/d	0 Kg/d
5	0 Kg/d	0 Kg/d
6	2155 Kg/d	1254 Kg/d
7	0 Kg/d	0 Kg/d
Total	2285 Kg/d	1457 Kg/d

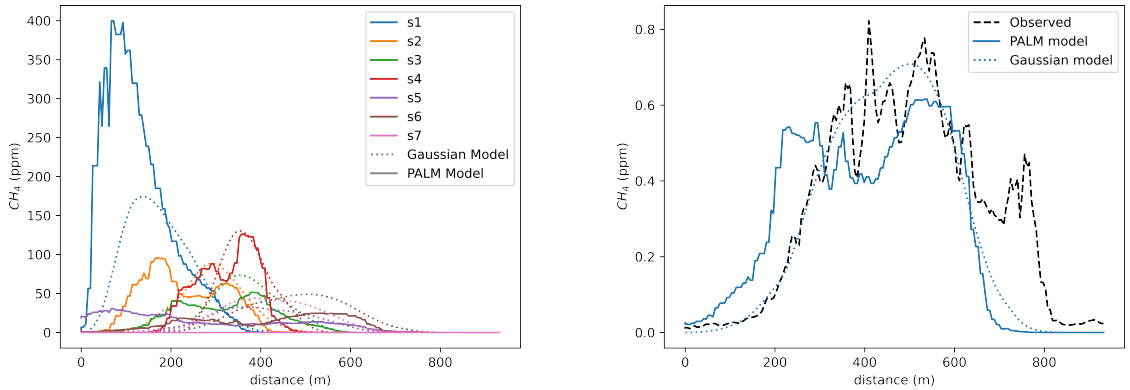

(a) (b)

Figure 5.6: 5.6a: representation of the contribution of each area source when the emission rate is normalized to 1 kg/s. The solid lines represent the PALM model, the dotted lines are for the Gaussian model. 5.6b: total concentration observed (black) and modelled (after the derivation of the optimal source rates) with the Gaussian model (blue dotted) and with the PALM model (blue solid). The lines obtained with the PALM model are jagged due to the 10 m grid used for the model setup.

Chapter 6

CONCLUSIONS AND PERSPECTIVES

We have started this work with a detailed study of two extensively used models for tracer transport: the Gaussian model and the PALM LES model. Our objective was to study their applicability in a system characterized by a complex topography and to understand if LES could give better results than the simple Gaussian model in such situations. A great effort was done in the study of the convergence of the LES with respect to execution time, grid size and domain size. The space of parameters of the PALM model was widely explored in order to obtain the best simulation setup, but there are still some settings that could be tried in future studies. Specifically, it would be of high interest to verify how the prediction of our LES would change with a different advection scheme and with the introduction of a pressure gradient. The quality of our emission plume simulation is highly influenced by our ability to reproduce the exact measured meteorological conditions. As we have seen, we still have large biases both in the wind direction and speed. There are many solutions that could be experimented to tackle this problem. One could try to bin the data by wind sectors and launch many simulations for different wind conditions instead of using an average wind. This will indeed increase the computational time, but it will produce a more precise result. A second option could be of using dynamical data as a meteorological forcing, in such a way one could run a single, but very costly, simulation with varying wind conditions. Another route that could be explored is of nudging the LES with a mesoscale meteorological analysis, such as one of those from the European center ECMWF. In addition, since the cyclic boundary conditions on the lateral axis cause a non natural periodicity in the flow, one could try to rotate the frame of reference for every wind condition in order to have always the wind velocity aligned with the horizontal axis. Finally, even if the chosen grid size is small enough from the point of view of the energy, it may not be suitable for representing well the details of the topography. Therefore, investing more computational resources by using a smaller grid size could increase the quality of our results. A last comment that can be done regarding the simulated wind filed, is that PALM is forced with winds at the inflow boundary, but the meteorological station at the landfill is approximately at the center of the domain. Thus the measured wind may simply be not well representative for our simulation.

Regarding the estimation of the methane emission sources, we have difference in the estimates using LES model and Gaussian model, but both models still provide the same order of magnitude and fit to concentration. We are confident that with more refining, through the possibilities stated above, the precision of the PALM model can become much higher than that of the Gaussian for landfill methane emissions. In such case, the choice of one model instead of the other must be subjected to a trade off between the desired quality and the computational time that we want to invest. We have seen in fact that the Gaussian model is already good at predicting the orders of magnitude of the

emission rates, with the great advantage of having a computational time of a few seconds instead of a day. Nevertheless, a great feature of LES is the possibility of producing high frequency data that can be compared with the observation. Here, we have not properly exploited this feature, as we have considered only average quantities that could also be calculated, and compared, with the Gaussian model, but their use should be the natural continuation to this research. Therefore, for this reason and for its potential precision, LES are a technique worth exploring for the estimation of landfill methane emissions.

Appendix A

Complements on the PALM LES model

We will here provide a description of all the variables and parameters cited in the PALM governing equations.

Table A.1: List of model variables.

Variables	
Symbol	Description
u_i	i$^{\text{th}}$ velocity component
x_i	i$^{\text{th}}$ spatial component
t	Time
$f_i = (0, 2\Omega\cos(\phi), 2\Omega\sin(\phi))$	Coriolis parameter
ϕ	Geographical latitude
$u_{g,i}$	i$^{\text{th}}$ geostrophic wind speeed component
$\pi^\star = p^\star + \frac{2}{3}\rho_0 e$	Modified perturbation pressure
$p^\star$	Perturbation pressure
$e = \frac{1}{2}\overline{u_i'' u_i''}$	SGS-TKE
$\theta = \frac{T}{\Pi}$	Potential temperature
T	Absolute temperature
$\Pi = \left(\frac{p}{p_0}\right)^{R_d/c_p}$	Exner function
p	Hydrostatic air pressure
$\theta_V = \theta\left[1 + \left(\frac{R_V}{R_d} - 1\right) q_V - q_l\right]$	Virtual potential temperature
q_l	Water specific humidity
Ψ_{q_V} Ψ_s	Source/sink of q_V and s
$K_m = c_m l\sqrt{e}$	Eddy diffusivity of momentum
$K_h = \left(1 + \frac{2l}{\Delta}\right) K_m$	Eddy diffusivity of heat
$\Delta = \sqrt[3]{\Delta x \Delta y \Delta z}$	Product of grid spacings
$l = \min\left(1.8z, \Delta, 0.76\sqrt{e}\left(\frac{g}{\theta_{V,0}}\frac{\partial\theta_V}{\partial z}\right)^{-\frac{1}{2}}\right)$ for $\frac{\partial\theta_V}{\partial z} > 0$	Mixing length
$l = \min(1.8z, \Delta)$ for $\frac{\partial\theta_V}{\partial z} \leq 0$	
ρ	Density of dry air

Table A.2: List of model parameters.

Parameters

Symbol	Value	Description
c_m	0.1	SGS model constant
c_p	1005 J kg^{-1} K^{-1}	Heat capacity of dry air at constant pressure
g	9.81 m s^{-2}	Gravitational acceleration
L_V	2.5×10^6 J kg^{-1}	Latent heat of vaporization
p_0	100 hPa	Reference air pressure
R_d	287 J kg^{-1} K^{-1}	Specific gas constant for dry air
R_V	461.51 J kg^{-1} K^{-1}	Specific gas constant for water vapor
κ	0.4	Kármán constant
ρ_0	1.0 kg m^{-3}	Density of dry air at the surface
$\rho_{l,0}$	1003 kg m^{-3}	Density of liquid water
Ω	0.729×10^{-4} rad s^{-1}	Angular velocity of the Earth

Appendix B

Description of a measurement campaign at the landfill

We present here a brief description of the measurement campaign performed on 14 and 15-06-2022. The modalities and the instruments are the same as the one used for the data that we have processed in this work.

Meteorological station

As anticipated, the meteorological data is stored through a 3D Sonic Anemometer placed 6.2 m above the ground. The instrument is installed approximately at the centre of the landfill, in order to measure data that can be representative for the whole site. At each measurement campaign the anemometer is realigned with the magnetic north. The alignment procedure, being practically complicated, is the one that can bring the largest uncertainties to the observations. One operator has to move the anemometer, while another has to check the correct alignment. In order to do so, the second operator must be at a distance of about 25 m to have a correct visual of the whole instrument. For this reason, the bias error in the wind direction can be as large as 4°. The anemometer is then fixed to the ground with ropes to avoid accidental rotations. In figure B.1 one can see a picture of the instrument installed at the landfill.

Figure B.1: 3D Sonic Anemometer installed in the center of the landfill.

Car mobile measurements

Mobile transects are are taken by driving a car on the roads in yellow in figure 3.2. The car is driven along those paths several times at a speed of about 20 km/h in order to cross the plumes. After that, all the plumes are combined according to the position in which they have been measured. In figure B.2 we present the instruments used.

(a) (b)

Figure B.2: B.2a: the air inlet (half bottle) is kept above the car for the whole measurement. B.2b: The inlet is connected to a LI-COR analyzer and to a GPS logger inside the car.

Sniffing measurements

During sniffing campaigns, the operator walks through all the site to manually sample the air and search for emission hotspots to insert in the model. The air inlet is kept at approximately 1 m above the ground and it is directly connected to a gas analyzer and a GPS logger. The time of measurements is corrected by the time the air takes to reach the analyzer from the inlet. In order to do so, before starting the measurements, the operator blows a few times in the inlet and stores the time of this operation. By checking the times of the measured peaks of CO_2, one can determine the correction factor. In figure B.3 we present the sniffing instrument and the results of the campaign.
As one can see from image B.3b and B.3c, the hotspots are very localized and it can become very difficult to locate them all in such a large area. Therefore, it is very likely to miss some sources when setting up the model.

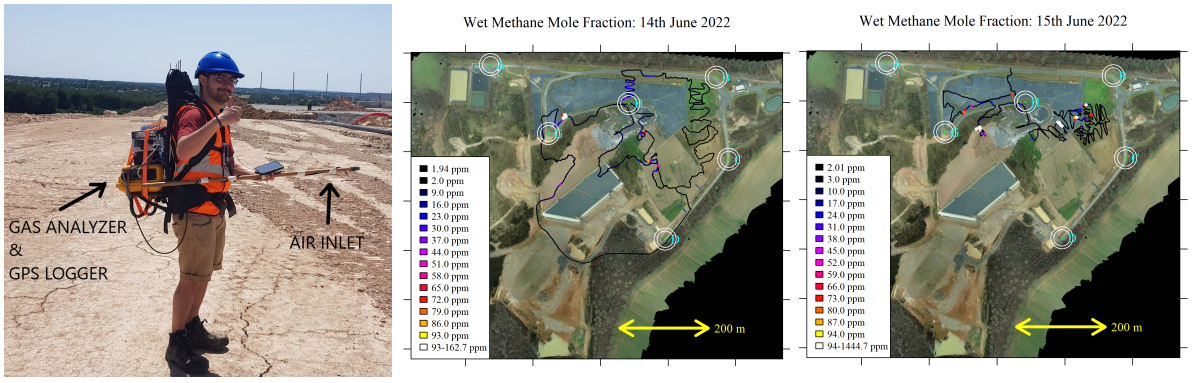

(a) (b) (c)

Figure B.3: B.3a: Sniffing instrumentation used on 14 and 15-06-2022 at the landfill. B.3b, B.3c: results from the sniffing campaign.

Appendix C

Summary on boundary conditions used in the simulations

Table C.1: Summary on boundary conditions used.

Quantity	Boundary	Condition
Flow field	inflow/outflow (X-axis)	Dirichlet/Neumann
Flow field	inflow/outflow (Y-axis)	cyclic
Tracer	inflow/outflow	Dirichlet/Neumann
Tracer	top/bottom	Neumann/Neumann
$p^\star$	top/bottom	Dirichlet/Neumann
θ	top/bottom	Dirichlet/Neumann
u, v	top/bottom	Dirichlet/No-slip

Bibliography

[1] John M. Stockie, "The Mathematics of Atmospheric Dispersion Modeling," *Society for Industrial and Applied Mathematics*, vol. 53, no. 2, pp. 349–372, 2011.

[2] Pramod Kumar, Grégoire Broquet et al., "Near-field atmospheric inversions for the localization and quantification of controlled methane releases using stationary and mobile measurements," *Royal Meteorological Society*, 2022.

[3] Stocker, T.F., D. Qin, G.-K. Plattner, M. Tignor, S.K. Allen, J. Boschung, A. Nauels, Y. Xia, V. Bex and P.M. Midgley (eds.), "IPCC Climate Change 2013: The Physical Science Basis. Contribution of Working Group I to the Fifth Assessment Report of the Intergovernmental Panel on Climate Change," 2013.

[4] L. H. Baker, W. J. Collins, D. J. L. Olivié, R. Cherian, Ø. Hodnebrog, G. Myhre, and J. Quaas, "Climate responses to anthropogenic emissions of short-lived climate pollutants," *Atmos. Chem. Phys.*, 2015.

[5] Euan G. Nisbet et al., "Methane on the Rise–Again," *Science*, 2014.

[6] Marielle Saunois et al., "The Global Methane Budget 2000–2017," *Earth Syst. Sci. Data*, 2020.

[7] P. Kumar, G. Broquet, C. Yver-Kwok, O. Laurent, S. Gichuki, C. Caldow, F. Cropley, T. Lauvaux, M. Ramonet, G. Berthe, F. Martin, O. Duclaux, C. Juery, C. Bouchet, and P. Ciais, "Mobile atmospheric measurements and local-scale inverse estimation of the location and rates of brief ch_4 and co_2 releases from point sources," *Atmospheric Measurement Techniques*, vol. 14, no. 9, pp. 5987–6003, 2021. [Online]. Available: https://amt.copernicus.org/articles/14/5987/2021/

[8] M. Hutchinson, H. Oh, and W.-H. Chen, "A review of source term estimation methods for atmospheric dispersion events using static or mobile sensors," *Information Fusion*, vol. 36, pp. 130–148, 2017. [Online]. Available: https://www.sciencedirect.com/science/article/pii/S156625351630152X

[9] Maronga, B., Gryschka, M., Heinze, R., Hoffmann, F., Kanani-Sühring, F., Keck, M., Ketelsen, K., Letzel, M. O., Sühring, M., and Raasch, S., "The Parallelized Large-Eddy Simulation Model (PALM) version 4.0 for atmospheric and oceanic flows: model formulation, recent developments, and future perspectives," *Geosci. Model Dev.*, vol. 8, pp. 1539–1637, 2015.

[10] B. Maronga, S. Banzhaf, C. Burmeister, T. Esch, R. Forkel, D. Fröhlich, V. Fuka, K. F. Gehrke, J. Geletič, S. Giersch, T. Gronemeier, G. Groß, W. Heldens, A. Hellsten, F. Hoffmann, A. Inagaki, E. Kadasch, F. Kanani-Sühring, K. Ketelsen, B. A. Khan, C. Knigge, H. Knoop, P. Krč, M. Kurppa, H. Maamari,

A. Matzarakis, M. Mauder, M. Pallasch, D. Pavlik, J. Pfafferott, J. Resler, S. Rissmann, E. Russo, M. Salim, M. Schrempf, J. Schwenkel, G. Seckmeyer, S. Schubert, M. Sühring, R. von Tils, L. Vollmer, S. Ward, B. Witha, H. Wurps, J. Zeidler, and S. Raasch, "Overview of the palm model system 6.0," *Geoscientific Model Development*, vol. 13, no. 3, pp. 1335–1372, 2020. [Online]. Available: https://gmd.copernicus.org/articles/13/1335/2020/

[11] Saiki, Eileen M., Moeng, Chin-Hoh, Sullivan, Peter P., "Large-Eddy Simulation Of The Stably Stratified Planetary Boundary Layer," *Boundary-Layer Meteorology*, vol. 95, pp. 1573–1472, 2000.

[12] S.E. Gryning and A.A.M. Holtslag and J.S. Irwin and B. Sivertsen, "Applied dispersion modelling based on meteorological scaling parameters," *Atmospheric Environment*, vol. 21, no. 1, pp. 79–89, 1987.

[13] R.R. Draxler, "Determination of atmospheric diffusion parameters," *Atmospheric Environment*, vol. 10, no. 2, pp. 99–105, 1976.

[14] Maithili Sharan and Pramod Kumar, "An analytical model for crosswind integrated concentrations released from a continuous source in a finite atmospheric boundary layer," *Atmospheric Environment*, vol. 43, no. 14, pp. 2268–2277, 2009.

[15] Dyer, A. J., "A review of flux-profile relationships," *Boundary-Layer Meteorology*, vol. 7, no. 3, pp. 1573–1472, 1974.

[16] Louis J. Wicker, William C. Skamarock, "Time-splitting methods for elastic models using forward time schemes," *Monthly Weather Review*, vol. 130, no. 8, pp. 2088–2097, 2002.

[17] W. Hackbusch, *Multi-Grid Methods and Applications*. Springer Berlin, Heidelberg, 1985. [Online]. Available: https://doi.org/10.1007/978-3-662-02427-0

[18] RICHARD C. SINGLETON, "An Algorithm for Computing the Mixed Radix Fast Fourier Transform," *IEEE TRANSACTIONS ON AUDIO AND ELECTROACOUSTICS*, vol. 17, no. 2, pp. 93–103, 1969.

[19] *WMO Guide to Meteorological Instruments and Methods of Observation*. World Meteorological Organization, 2008.

[20] MARGARET F. J. WILSON, BRIAN O'CONNELL, COLIN BROWN, JANINE C. GUINAN, AND ANTHONY J. GREHAN, "Multiscale Terrain Analysis of Multibeam Bathymetry Data for Habitat Mapping on the Continental Slope," *Marine Geodesy*, vol. 30, no. 1-2, pp. 3–35, 2007.

[21] J. Steven R. Hanna Gary A. Briggs Rayford P. Hosker, *Handbook on ATMOSPHERIC DIFFUSION*. TECHNICAL INFORMATION CENTER U.S. DEPARTMENT OF ENERGY, 1982.